Volumen 11 número 30 enero-abril 2025

UJAT
UNIVERSIDAD JUÁREZ AUTÓNOMA DE TABASCO

"ESTUDIO EN LA DUDA. ACCIÓN EN LA FE"

# JOBS
## Journal of Basic Sciences

DACB · UJAT

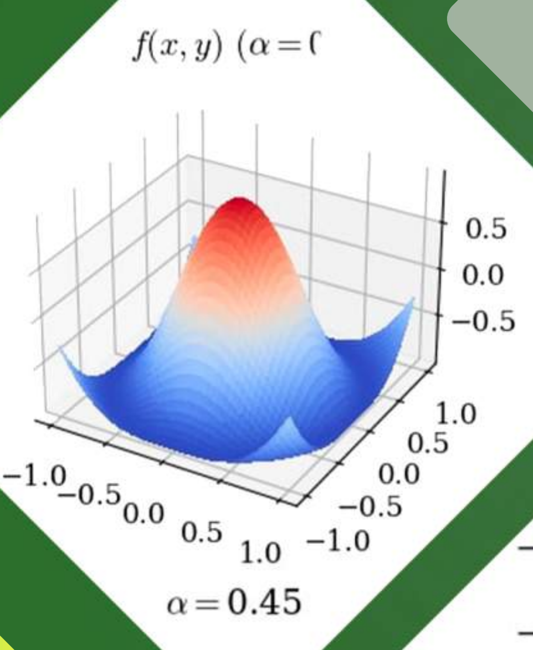


División Académica de Ciencias BÁSICAS UJAT

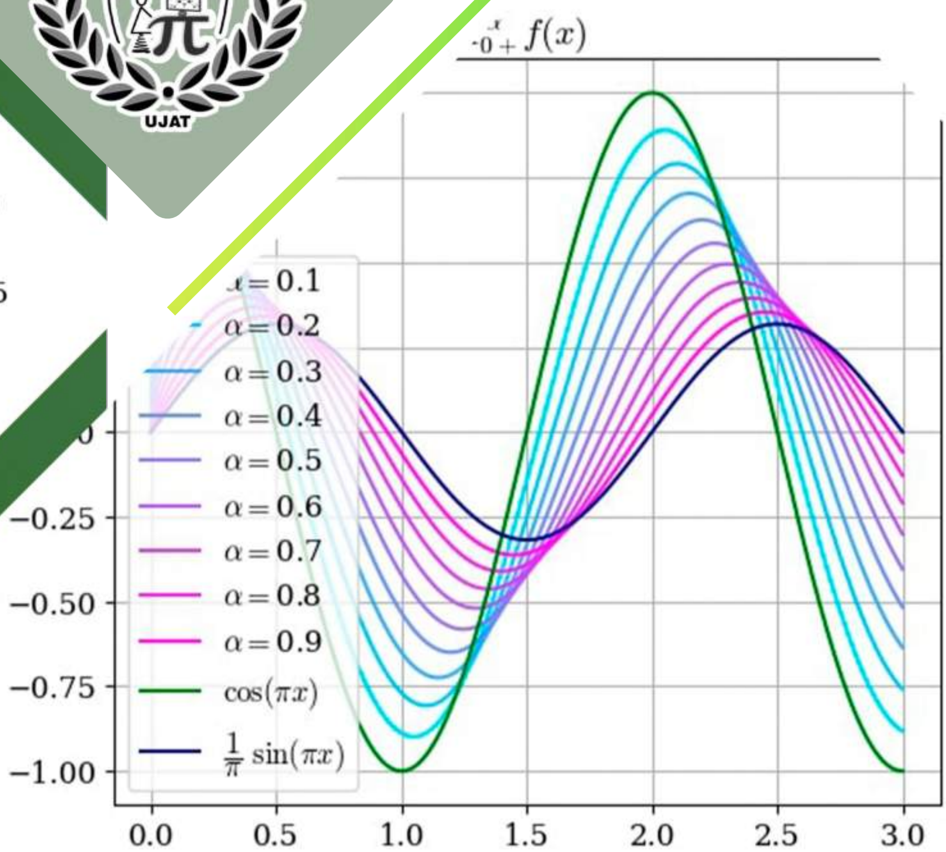


ISSN:2448-4997
https://revistas.ujat.mx/index.php/jobs

UJAT
Universidad Juárez Autónoma de Tabasco
"Estudio en la duda. Acción en la fe"
JOBS Journal of Basic Sciences

Con el número 30 del Journal of Basic Sciences, se inicia el volumen 11 de esta revista correspondiente al año 2025. El carácter multidisciplinario de esta revista, permite enriquecer su contenido con perspectivas variadas que abordan diversas problemáticas en el área de las ciencias básicas y disciplinas afines.

De esta forma, se presenta una contribución que desarrolló generalizaciones en cálculo multivariable para llegar a nuevas diferenciales totales fraccionarias, las cuales juegan un papel importante en la modelación de gran número de fenómenos. Por otro lado, se incluye también una aportación que trata sobre el desarrollo de un método para resolver la ecuación de transporte conservativa en dominios específicos, incluyendo su validación y prueba para demostrar sus capacidades.

Se incluye además, un reporte encaminado a mejorar la calidad de imágenes, mediante técnicas de discretización numérica presentando una evaluación cualitativa y cuantitativa de los resultados obtenidos. En otro orden de ideas, se centra la atención hacia el estudio de sistemas aleatorios y la complejidad en su modelación, mostrando un estudio inferencial para un proceso de Poisson mixto, que lleva a la obtención de expresiones para densidad predictiva.

Es innegable que el aprendizaje de las matemáticas representa un reto actual que no debe soslayarse. En este sentido, se incluye un estudio que muestra la relación entre el desarrollo de la memoria de trabajo y el aprendizaje de identidades trigonométricas por parte de jóvenes del nivel medio superior, mostrando los subcomponentes necesarios en el razonamiento para el aprendizaje de este tema. En otra contribución relativa a la matemática educativa, se presenta una propuesta para atender el aprendizaje de los polígonos por estudiantes de bachillerato, mediante una serie de actividades diseñadas ex profeso que permiten una mejora en la comprensión de la temática.

En un contexto diferente, está el estudio dirigido a evaluar la actividad antibacteriana de extractos de plantas del género Cecropia, de uso tradicional en el sureste mexicano, correlacionando esta propiedad con el perfil fitoquímico analizado. Se presenta además, una contribución encaminada a analizar el impacto, que en los últimos años, han ocasionado derrames petroleros en el sureste mexicano, con especial énfasis en la afectación a cultivos agrícolas.

La atención de problemas de salud está dada a través de dos artículos que forman parte de este número. Por un lado, se comparó la resistencia a la insulina a través de índices específicos en momentos anteriores y durante la pandemia de COVID-19; en otro aporte, se analiza la relación entre diversos factores de riesgo asociados a la población joven y la enfermedad de Chagas. Mientras que en el área de la ciencia de los materiales, se incluye una propuesta para la obtención de derivados de poliuretano, con un método eficiente y compacto.

De esta forma el Journal of Basic Sciences acerca a sus lectores al amplio panorama del quehacer científico.

# DIRECTORIO INSTITUCIONAL

**Universidad Juárez Autónoma de Tabasco**

Lic. Guillermo Narváez Osorio.
Rector

Dr. Luis Manuel Hernández Govea.
Secretario de Servicios Académicos

Dr. Wilfrido Miguel Contreras Sánchez.
Secretario de Investigación, Posgrado y Vinculación

Dr. Pablo Marín Olán. Director de Difusión,
Divulgación Científica y Tecnológica

**Directorio Divisional**
**División Académica de Ciencias Básicas**

Dra. Hermicenda Pérez Vidal.
Directora

Dr. Luis Manuel Martínez González.
Coordinador de Investigación

M.C. Abel Cortazar May.
Coordinador de Docencia

L.Q. Esmeralda León Ramos.
Coordinador de Difusión Cultural y Extensión

UJAT
UNIVERSIDAD JUÁREZ AUTÓNOMA DE TABASCO
"ESTUDIO EN LA DUDA. ACCIÓN EN LA FE"

# CONSEJO EDITORIAL



# COMITÉ EDITORIAL




JOURNAL OF BASIC SCIENCES, Vol. 11, Núm. 30, abril de 2025, es una publicación continua cuatrimestral, editada por la División Académica de Ciencias Básicas de la Universidad Juárez Autónoma de Tabasco, Av. Universidad S/N, Zona de la Cultura, Col. Magisterial, C.P. 86040, Villahermosa Tabasco, México. Tel. (+52) (933) 358 1500 Ext. 5040. https://revistas.ujat.mx/index.php/jobs. Editor Responsable de la Revista: Carlos Ernesto Lobato García. Reserva de derechos al uso exclusivo 04-2015-052110084000-203, ISSN: 2448-4997, ambos otorgado por el Instituto Nacional del Derecho de Autor. Universidad Juárez Autónoma de Tabasco, Av. Universidad S/N, Zona de la Cultura, Col. Magisterial, Centro, Tabasco. C.P. 86040. Fecha de última actualización, 30 de enero de 2025.

# CONTENIDO



ISSN:2448-4997
https://revistas.ujat.mx/index.php/jobs

ISSN:2448-4997
https://revistas.ujat.mx/index.php/jobs

Vol. 11(30), p. 16–31, enero-abril 2025, e-ISSN: 2448-4997
JOURNAL OF BASIC SCIENCES

# An unstructured finite-volume method for the two-dimensional conservative transport equation

**Itzá Balam, Reymundo**[1,2*], **Uh Zapata, Miguel**[1,2]
[1] *Secretaría de Ciencia, Humanidades, Tecnología e Innovación (SECIHTI), México.*
[2] *Centro de Investigación en Matemáticas A.C. (CIMAT), Unidad Mérida, PCTY, Sierra Papacal, C.P. 97302, Mérida, Yucatán, México*
[*] *reymundo.itza@cimat.mx*

**Resumen**

En este artículo presentamos un método de segundo orden de precisión tanto temporal como espacial, para resolver la ecuación de transporte conservativa en dominios bidimensionales. La discretización espacial se basa en un enfoque de volumen finito que utiliza celdas triangulares arbitrarias. Se emplea el método $\theta$ para la integración temporal. Se propone un esquema de segundo orden del tipo *upwind* con una formulación de limitador de flujo para la disminución de extremos locales para aproximar los términos advectivos. El método numérico se valida con casos de prueba clásicos de advección, que incluyen diferentes funciones características y tipos de mallas. Finalmente, se realizan varias pruebas para demostrar las capacidades del esquema propuesto.

***Palabras claves***: *Método de volúmenes finitos, ecuación de transporte conservativa, malla no estructurada, esquema upwind, segundo orden de precision, limitador de flujo.*

**Abstract**

In this paper, we present a second-order, time- and space-accurate method for solving conservative transport equation in two-dimensional domains. The spatial discretization is based on a finite volume approach using triangular cells of arbitrary shape. A $\theta$-method is employed for the time integration. A second-order upwind scheme with a Local Extremum Diminishing flux limiter formulation is proposed to approximate the advective terms. The numerical method is validated against classical advection test cases, including different characteristic functions and type of grids. Finally, several tests are conducted to demonstrate the capabilities of the proposed scheme.

***Keywords***:*Finite-volume method, conservative transport equation, unstructured grid, upwind scheme, second order of accuracy, flux limiter.*

Recibido: 7 de noviembre de 2024. Aceptado: 29 de enero de 2025. Publicado: 30 de abril de 2025.

# 1 Introduction

A wide range of natural and industrial applications involve the conservative transport equation [1]. In fluid mechanics, for example, it plays a crucial role in solving the Navier-Stokes equations. Additionally, it is essential for modeling multi-phase flows employing interface-capturing methods such as the level set method [2, 3, 4, 5]. In general, interface-capturing methods are based on the spatial discretization of a characteristic function to distinguish between two regions, and the position of the interface is computed at each time step by solving an advection equation.

On the other hand, unstructured grids allow applications to geophysical flows of arbitrary two-dimensional (2D) geometries with the presence of many obstacles, which is in general hard to achieve on structured grids. Most of the methods used for the transport equation with unstructured grids have been developed in the framework of finite-element method. However, the finite-volume method (FVM) is attractive due to its local conservation property, which is not the case for standard finite-difference or finite-element methods.

The literature that involve numerical interface-capturing methods applying a finite-volume approach is limited on unstructured grids [6, 7, 8, 9]. Motivated by this gap, the present work aims to investigate a FVM on arbitrarily triangular shaped cells for solving the conservative transport equation on $\Omega$:

$$\frac{\partial \phi}{\partial t} + \nabla \cdot (\mathbf{u}\phi) = 0, \tag{1}$$

where $\phi$ is the unknown variable, $t$ is the time, and $\mathbf{u}$ is the known velocity field.

In general, accurate approximations of equation (1) are not simple to obtain due to different difficulties such as false diffusion, non-conservative, overshoot/undershoot and phase error [10]. In order to mitigate the diffusion effect, second-order schemes must be employed. Central schemes performs well in smooth scenarios; however, they produce numerical solutions with oscillations around sharp regions. On the other hand, second-order upwind schemes work well near discontinuities but oscillations still exist which can be reduce or eliminate by the introduction of a flux-limiter technique [10].

In this paper, we present a second-order accurate and robust numerical method for equation (1). The time integration is based on a $\theta$-method which allow us to select between an explicit, implicit or Crank-Nicolson (semi-implict) formulation. The space discretization is based on a finite-volume method on unstructured triangular grids. In contrast with other formulations [8], the proposed advective approximation is based on a second-order upwind interpolation scheme. The corresponding gradients are calculated using a least square technique [11]. In order to eliminate non-desirable oscillations, the approximations also incorporate a flux limiter which is determined by the Local Extremum Diminishing (LED) technique [12].

This paper is organized as follows. The second section introduces the time integration. The third section presents the finite-volume discretization on triangular grids. The fourth section discuss the final approximation and the linear solver employed to its solution. Next, the numerical techniques are tested over different benchmark problems. Finally, last section includes the conclusions and ideas to be pursued in future work.

# 2 Time integration: $\theta$-method

Depending on how the advective term is approximated, either explicit or implicit numerical methods can be employed. If the advective term is evaluated at time $t^n$, a simple forward approximation for the time derivative yields a first-order time-accurate explicit scheme for equation (1) given by:

$$\frac{\phi^{n+1}-\phi^n}{\Delta t}+\nabla\cdot(\phi^n\mathbf{u}^n)=0, \tag{2}$$

where $\Delta t$ is the computational time step, and $n$ denotes the time level. However, the time step, and thus the stability region, of the explicit scheme is constrained by the Courant-Friedrichs-Lewy (CFL) condition. To avoid this time-step restriction, an implicit formulation can be used by evaluating the advective term at time $t^{n+1}$, as follows:

$$\frac{\phi^{n+1}-\phi^n}{\Delta t}+\nabla\cdot\left(\phi^{n+1}\mathbf{u}^{n+1}\right)=0, \tag{3}$$

While this implicit approach eliminates the stability constraint, it still results in a first-order time-accurate approximation. In this study, we also introduce a second-order semi-implicit time-advancement scheme based on the Crank-Nicolson (C-N) method:

$$\frac{\phi^{n+1}-\phi^n}{\Delta t}+\nabla\cdot\left(\frac{1}{2}\phi^{n+1}\mathbf{u}^{n+1}+\frac{1}{2}\phi^n\mathbf{u}^n\right)=0. \tag{4}$$

Thus, the time-advancement schemes (2), (3), and (4) for the advection equation can be summarized as follows:

$$\phi^{n+1}+\theta\Delta t\nabla\cdot\left(\phi^{n+1}\mathbf{u}^{n+1}\right)=\phi^n-(1-\theta)\Delta t\nabla\cdot\left(\phi^n\mathbf{u}^n\right), \tag{5}$$

where $\theta$ is equal to 0, 1 or 1/2 if the method is explicit, implicit or Crank-Nicolson, respectively. We remark that $\mathbf{u}$ is always known at any time step.

## 3 Space discretization: finite volume method

The 2D computational domain is discretized into $N_V$ triangular cells. For each triangle control volume $V_i$, we denote as $L_j$ ($j=1,2,3$) to its three edges. We use a staggered grid and then the face-normal velocity $U=\mathbf{u}\cdot\mathbf{n}$ and variable $\phi$ are located at the centers of the cell edges, $\mathbf{x}_{ij}=(x_{ij},y_{ij})$, and the cell-centered point $\mathbf{x}_i=(x_i,y_i)$ of the cell, respectively. Here, $\mathbf{n}$ denotes the outward normal unit vector at each edge. A schematic plot of the triangular element and its components is shown in Fig. 1.

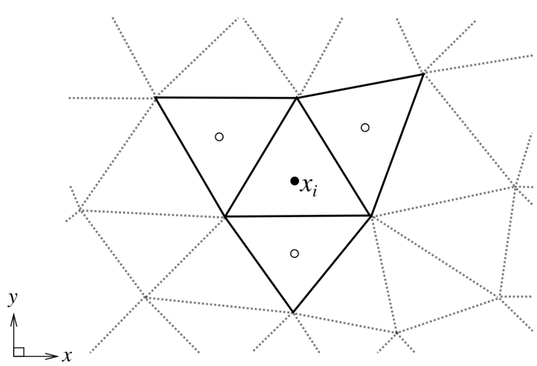


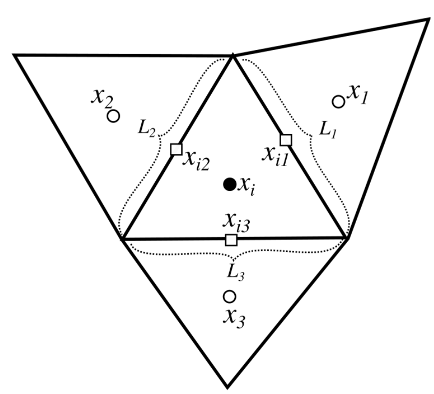


Figure 1: Sketch of the two-dimensional control volume $V_i$ and its three edges $L_j$ ($j=1,2,3$) used for the finite volume discretization.

Following the standard finite-volume formulation, equation (5) is integrated over each control volume $V_i$, which formally gives (assuming sufficient regularity) the following balance equation:

$$\iint\limits_{V_i} \phi^{n+1} dV + \theta\Delta t \iint\limits_{V_i} \nabla \cdot \left(\phi^{n+1}\mathbf{u}^{n+1}\right) dV = \iint\limits_{V_i} \phi^{n} dV - (1-\theta)\Delta t \iint\limits_{V_i} \nabla \cdot \left(\phi^{n}\mathbf{u}^{n}\right) dV.$$

After application of the Green's Theorem, one obtains

$$\iint\limits_{V_i} \phi^{n+1} dV + \theta\Delta t \sum_{j=1}^{3} \oint\limits_{L_j} \left(\phi^{n+1}\mathbf{u}^{n+1}\right) \cdot \mathbf{n} dl = \iint\limits_{V_i} \phi^{n} dV - (1-\theta)\Delta t \sum_{j=1}^{3} \oint\limits_{L_j} \left(\phi^{n}\mathbf{u}^{n}\right) \cdot \mathbf{n} dl. \tag{6}$$

Here, the index $j$ refers to the edge $L_j$ of the control volume $V_j$, which shares this side with $V_i$. It should be noted that up to this point we haven't introduced any spacial approximation.

### 3.1 Integral approximations

A second-order scheme is obtained from (6) by applying the midpoint rule integral approximation for the triangular element and its corresponding edges. Thus, we get

$$m_{V_i}\phi_i^{n+1} + \theta\Delta t \sum_{j=1}^{3} m_{L_j} \left(\phi^{n+1}\mathbf{u}^{n+1}\right)_{ij} \cdot \mathbf{n}_j = m_{V_i}\phi_i^{n} - (1-\theta)\Delta t \sum_{j=1}^{3} m_{L_j} \left(\phi^{n}\mathbf{u}^{n}\right)_{ij} \cdot \mathbf{n}_j, \tag{7}$$

where $(\cdot)_{ij}$ denotes the evaluation of a variable at $\mathbf{x}_{ij}$, the midpoint of $L_j$, as shown in Fig. 1. We denote as $m_{V_i}$ and $m_{L_j}$ the area of $V_i$ and the length of $L_j$, respectively. The outward normal unit vector directed from $V_i$ to $V_j$ is defined as $\mathbf{n}_j$. Finally, we can rewrite equation (7) as follows:

$$\phi_i^{n+1} + \theta r_i \sum_{j=1}^{3} m_{L_j}\phi_{ij}^{n+1}U_{ij}^{n+1} = \phi_i^{n} - (1-\theta) r_i \sum_{j=1}^{3} m_{L_j}\phi_{ij}^{n}U_{ij}^{n}, \tag{8}$$

where $r_i = \Delta t / m_{V_i}$ and the normal-face flux crossing the face of the two control volume is given by

$$U_{ij} = (\mathbf{u}\cdot\mathbf{n})_{ij}, \quad j = 1, 2, 3,$$

for the new and current time step. As we know the velocity field is known, the discretization is complete by approximating $\phi_{ij}$ in equation (8) as a function of the discrete unknowns $\phi_i$ and $\phi_j$ associated to each control volume $V_i$ and its neighbors $V_j$, respectively.

### 3.2 Upwind scheme

In equation (8), the advective term is approximated using an upwind scheme around the point $\mathbf{x}_{ij}$, as follows [13]:

$$\phi_{ij} \approx \begin{cases} \phi_{ij}(V_i), & U_{ij} \geq 0, \\ \phi_{ij}(V_j), & U_{ij} < 0, \end{cases} \qquad j = 1, 2, 3, \tag{9}$$

where $\phi_{ij}(V_i)$ and $\phi_{ij}(V_j)$ represent the approximations of $\phi_{ij}$ at the face shared by the adjacent control volumes $V_i$ and $V_j$, respectively. Thus, the unknown variable $\phi_{ij}$ in (9) at the mid-point of the edges can be approximated in several ways, and the accuracy of the numerical method depends on the precision of this interpolation.

A first-order approximation at the edge is obtained by simple taking the values at the cell-centered points:

$$\phi_{ij}(V_i) = \phi_i,$$
$$\phi_{ij}(V_j) = \phi_j.$$

This approximation can be improved to a second-order approximation at the edge using Taylor expansions, as follows:

$$\begin{aligned}\phi_{ij}(V_i) &= \phi_i + \nabla\phi_i \cdot (\mathbf{x}_{ij} - \mathbf{x}_i),\\ \phi_{ij}(V_j) &= \phi_j + \nabla\phi_j \cdot (\mathbf{x}_{ij} - \mathbf{x}_j).\end{aligned} \tag{10}$$

However, as discussed in the numerical examples, the approximation in (10) introduces additional errors when the solution lacks smoothness.

Note that gradient approximations are required to reach a second-order of accuracy. We use a least square technique as described in the work of Lien [11]. In this method, the solution is assumed to be linear in each control volume $\phi(x, y) = ax + by + c$, such that $\nabla\phi = (a, b)$. The coefficients $a$ and $b$ are determined using the values $\phi_i$ and the neighbors $\phi_j$ $(j = 1, 2, 3)$. Although, the resulting gradient approximation is only first-order accurate, equation (10) results in a second-order approximation.

### 3.3 Upwind scheme with a flux-limiter technique

In order to eliminate non-desirable oscillations, flux limiters $\psi_i$ and $\psi_j$ can be incorporated into equation (10) to obtain

$$\phi_{ij}(V_i) = \phi_i + \psi_i\nabla\phi_i \cdot (\mathbf{x}_{ij} - \mathbf{x}_i),$$
$$\phi_{ij}(V_j) = \phi_j + \psi_j\nabla\phi_j \cdot (\mathbf{x}_{ij} - \mathbf{x}_j),$$

where $\psi_i$ and $\psi_j$ are determined by the Local Extremum Diminishing technique [12] satisfying

$$\phi_{\min} \le \phi_{ij} \le \phi_{\max},$$

where $\phi_{\min}$ and $\phi_{\max}$ are the minimum and the maximum taken over $V_i$ and its surrounding neighbors. A unique value of the flux limiter per control volume $V_i$ is determined as

$$\psi_i = \min(\psi_{i1}, \psi_{i2}, \psi_{i3}),$$

where

$$\psi_{ij} = \begin{cases} \min\left(1, \frac{1}{\Theta_i}\left[\phi_{\max} - \phi_j\right]\right), & \text{if } \Theta_i > 0,\\ \min\left(1, \frac{1}{\Theta_i}\left[\phi_{\min} - \phi_j\right]\right), & \text{if } \Theta_i < 0,\\ 1, & \text{if } \Theta_i = 0. \end{cases}, \qquad j = 1, 2, 3,$$

and $\Theta_i = \nabla\phi_i \cdot (\mathbf{x}_{ij} - \mathbf{x}_i)$. This technique ensures that local maximum cannot increase and local minimum cannot decrease.

## 4 Final linear system and solver

In summary, a finite volume discretization of equation (1) at each control volume $V_i$ results in the linear system of equations

$$\phi_i^{n+1} + \theta r_i \left( a_0\phi_i^{n+1} + \sum_{j=1}^{3} a_j\phi_j^{n+1} + a_G^{n+1} \right) = f_i^n, \qquad i = 1, 2, \ldots, N_V, \tag{11}$$

where $f_i^n$ is the right-hand side given by

$$f_i^n = \phi_i^n - (1-\theta) r_i \left( a_0 \phi_i^n + \sum_{j=1}^{3} a_j \phi_j^n + a_G^n \right), \qquad i = 1, 2, \ldots, N_V. \tag{12}$$

The coefficients corresponding to the upwind scheme (11)-(12) are given by

$$a_1 = \min(U_{i1}, 0), \qquad a_2 = \min(U_{i2}, 0), \qquad a_3 = \min(U_{i3}, 0), \qquad a_0 = a_1 + a_2 + a_3,$$

and $a_G$ includes all the terms related with the gradient approximation and flux limiter technique.

Boundary conditions are included into the problem as updates of ghost values. Let us denote $\phi_g$ the corresponding ghost cell of $\phi_i$. Dirichlet boundary conditions are updated as the average of both values resulting in $\phi_g = 2\phi_{exact} - \phi_i$, where $\phi_{exact}$ is the corresponding known values at the boundary. Figure 2 illustrates the implementation of the Dirichlet boundary condition using ghost cells.

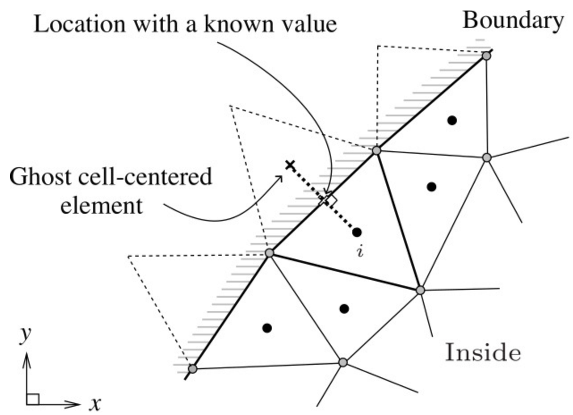


Figure 2: Sketch of the Dirichlet boundary condition and the ghost values used to apply these conditions.

Besides the explicit formulation, equation (11) results in a linear system of the form

$$A\vec{\phi} + \vec{b}_{\phi} = \vec{f}, \tag{13}$$

where $\vec{\phi}$ consists of the unknown variables, the matrix $A$ only contains the coefficients obtained from the geometric values and the known velocity field, $\vec{b}_{\boldsymbol{\phi}}$ contains all the values related to the gradient at the new time step, and $\vec{f}$ corresponds to the known right-hand side given by (12). It is important to remark that the components of $\vec{b}_{\phi}$ relates more values than the ones located at $V_i$ and its neighbors $V_j$. This significantly complicate the computer implementation. In order to simplify this problem, $\vec{b}_{\phi}$ is not explicitly calculated by the linear solver, as explained below.

The efficiency of the scheme depends on the selection of the solver for linear system (13). Many solvers can be chosen; however, in reason of their efficiency and simplicity in implementation, we consider a classical stationary iterative methods, the Gauss-Seidel (GS) method. It solves the new time step using previous value for $\vec{\phi}$ as follows

$$(D+L)\vec{\phi}^{(k+1)} = \left(\vec{f} - \vec{b}_{\phi}^{(k)}\right) - U\vec{\phi}^{(k)}, \tag{14}$$

where $L$, $U$ and $D$ are the lower, upper and diagonal matrices of $A$, respectively; superscripts $(k)$ and $(k+1)$ indicates the values of the previous and current iteration, respectively. There are some important characteristics of equation (14) that should be noted. First, the GS method is not exactly the same as their original definition because of $\overrightarrow{b}_{\phi}^{(k)}$. This vector should include some values corresponding to $(k+1)$ but all are updated using the previous iteration. Second, the gradient should be updated at each iteration to obtain $\overrightarrow{b}_{\phi}^{(k)}$.

# 5 Numerical results

For the numerical results, we present some numerical simulations that explore some important features of the proposed formulation, which include temporal and spatial accuracy. The accuracy of the method is quantified using different initial functions, grid types and grid resolutions. The 2D solid-body rotation example is used to test the transport equation. In all the cases, linear systems have been solved using the Gauss-Seidel solver with a tolerance value of $10^{-8}$.

## 5.1 The solid-body rotation problem

For the example, we consider the conservative transport problem given by

$$\begin{aligned} \frac{\partial \phi}{\partial t} + \nabla \cdot (2\pi(-y,x)\phi) &= 0, & (x,y) &\in \Omega, \\ \phi(x,y,0) &= \phi_0(x,y), & (x,y) &\in \Omega. \end{aligned}$$

where the computational domain is the square $\Omega = [-1,1]\times[-1,1]$. Here, the velocity $\mathbf{u} = 2\pi(-y,x)$ has been chosen such that one full revolution takes place within final time $t = 1$. Therefore, the exact solution of the problem at $t = 1$ is the same as the initial condition. Thus, the error $E$ is calculated as the absolute difference between the numerical and exact solution. Furthermore, the order of accuracy is calculated as order $= \log\left(\|E\|_{N_1} / \|E\|_{N_2}\right) / \log\left(N_2/N_1\right)$, where $\|E\|_{N_1}$ and $\|E\|_{N_2}$ can be the $L_\infty$- or $L_2$-norm error with resolutions $N_1$ and $N_2$.

In order to study the effect of the regularity of the numerical solution, we consider three different initial conditions. They are given by

$$\text{Example 1}: \qquad \phi_0(x,y) = \begin{cases} \cos^2(2\pi r), & r \le r_0, \\ 0, & r > r_0, \end{cases}$$

$$\text{Example 2}: \qquad \phi_0(x,y) = \begin{cases} \cos(2\pi r), & r \le r_0, \\ 0, & r > r_0, \end{cases}$$

$$\text{Example 3}: \qquad \phi_0(x,y) = \begin{cases} 1, & r \le r_0, \\ 0, & r > r_0, \end{cases}$$

where $r = \sqrt{(x-x_0)^2 + (y-y_0)^2}$, $r_0 = 1/4$ and $(x_0, y_0) = (-1/2, 0)$, see Fig. 3. The first initial condition is the well-known cosine-bell example and it corresponds to a $C^1$ function. For the second initial condition, the function is continuous but not derivable at $r = r_0$. Finally, in the third example, the initial condition corresponds to a discontinuous function at $r = r_0$. Homogeneous Dirichlet conditions are imposed at all boundaries.

## 5.2 Structured and unstructured triangular grids

Structured and unstructured grids are employed for the numerical simulations. For structured grids, the domain is firstly divided into equilateral triangles, see Fig. 4(a). Next, right-angled grids

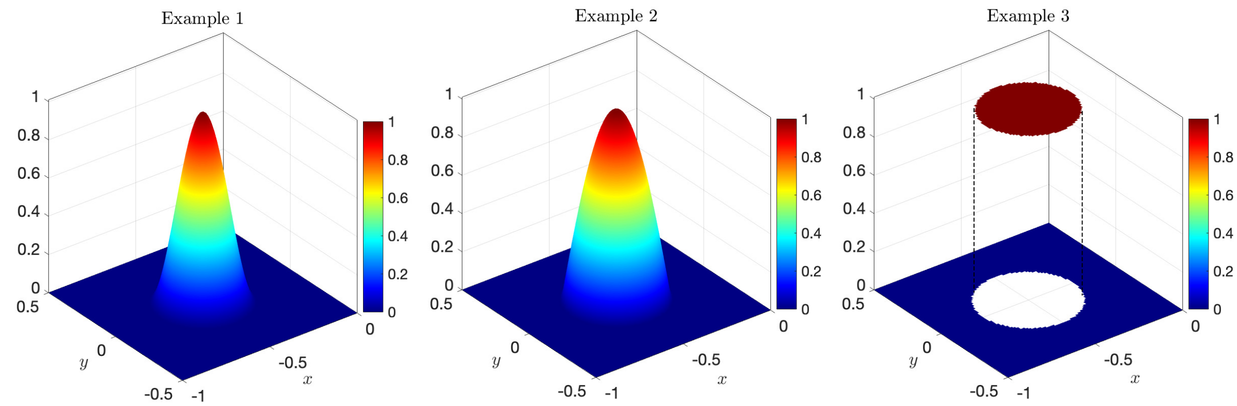


Figure 3: Initial conditions used in the solid-body rotation simulations.

are obtained from $(N_x - 1) \times (N_y - 1)$ uniform rectangles divided into two triangles, as shown in Fig. 4(b). For unstructured grids, not only triangles change size, but also the number of triangles sharing a particular node is different, as shown in Fig. 4(c). Unstructured grids have been generated using the free software Blue Kenue developed by the Canadian Hydraulic Centre, National Research Council (1998).

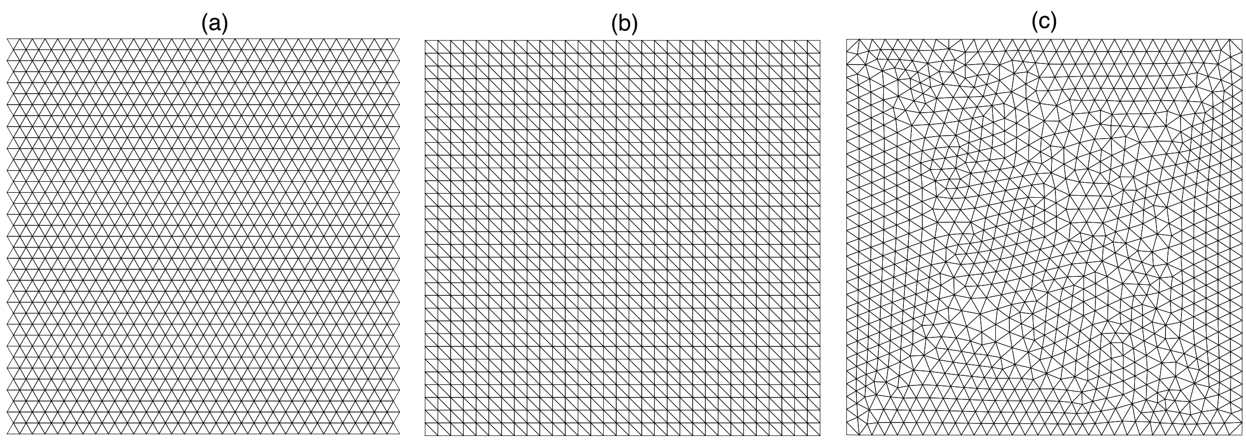


Figure 4: (a) Equilateral, (b) right-angled, and (c) unstructured triangular grids with $\Delta x = 0.0625$.

Table 1 shows the number of vertex and cell-centered points used to discretize a square of resolution $N = N_x = N_y$. Here, $\Delta x = L/(N_x - 1)$ is the length of the triangle in the $x$-direction, where $L = 2$ is the 2D domain width. For unstructured grids, the mesh was generated by taking a mean triangle edge close to the corresponding $\Delta x$.

Table 1: Size of the structured and unstructured grids used in numerical experiments for the computational domain.

| Grid | | Equilateral | | Right-angled | | Unstructured | |
|---|---|---|---|---|---|---|---|
| $N$ | $\Delta x$ | Vertices | Cells | Vertices | Cells | Vertices | Cells |
| 32 | 0.0625 | 1,116 | 2,196 | 1,024 | 1,922 | 1,188 | 2,234 |
| 64 | 0.03125 | 4,636 | 9,000 | 4,096 | 7,938 | 4,752 | 9,234 |
| 128 | 0.015625 | 18,743 | 36,938 | 16,384 | 32,258 | 18,355 | 36,121 |
| 256 | 0.0078125 | 75,373 | 149,646 | 65,536 | 130,050 | 72,351 | 143,473 |

### 5.3 Preservation of the initial condition's shape

The effectiveness of the proposed numerical method can be initially addressed by examining how well the initial condition's shape is preserved during its transport. Figure 5 illustrates the numerical solution using the cosine-bell initial condition, see Example 1. Here, we show the velocity field and contours of the numerical solution at six stages: $t = 0$, 0.2, 0.4, 0.6, 0.8, and 1 using the upwind-scheme, $\Delta t = 10^{-4}$, and the right-angled structured grid with resolution $N = 256$. The black circle in all images corresponds to the contour level at $\phi = 1/4$. Notice that the numerical solution nicely preserves the round shape of the initial conditions.

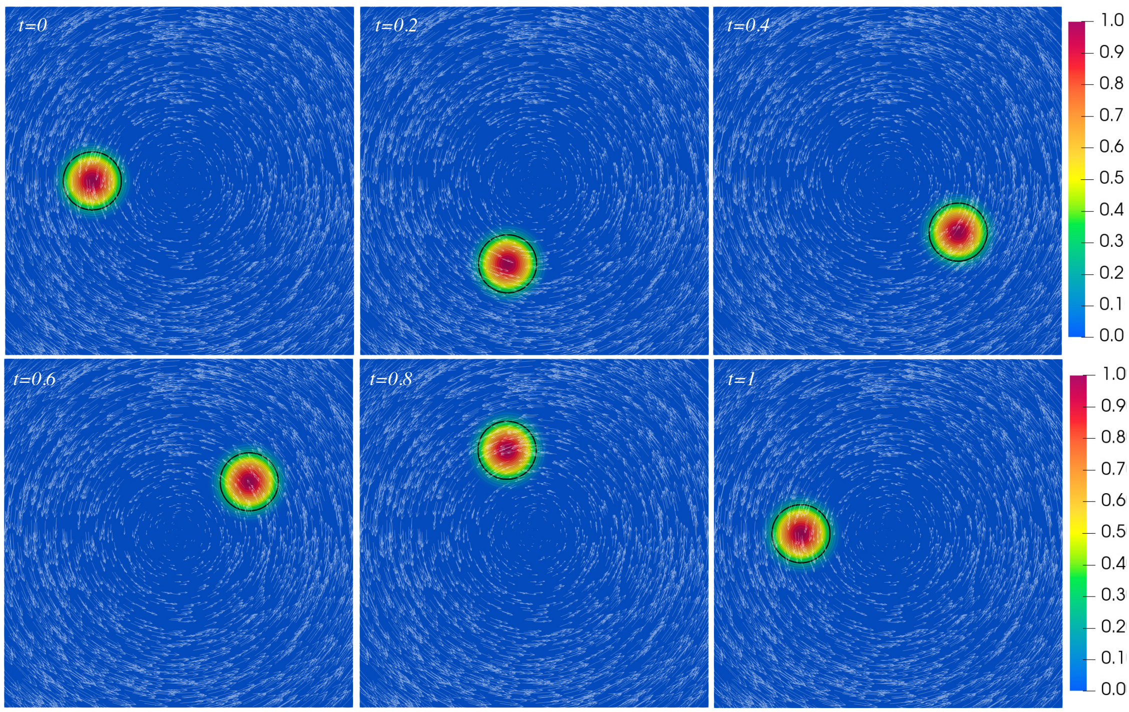


Figure 5: Velocity field and numerical solution of Example 1 at six stages using a right-angled structured grid with resolution $N = 256$.

The numerical solution using the three different initial conditions is presented in Fig. 6. We plot only the solution in the region $[-1, 0] \times [-0.5, 0.5]$ where the non-zero $\phi$ values are located. As expected, the numerical solution still preserves the round shape of the initial conditions for all cases. Note that the error increases as the the regularity of the solution decreases. For instance, undesired oscillations arise in the discontinuous case due to the second-order approximation used in our scheme.

On the other hand, Fig. 7 and Fig. 8 present the numerical solution at $t = 1$ using the cosine-bell initial condition using structured and unstructured triangular grids, each with a resolution of $N = 256$. Notice the impact of the unstructured triangular grid on the numerical solution. Further details on the errors are provided in the next section.

### 5.4 Temporal and space accuracy

Temporal accuracy is investigated by varying the time step while keeping the grid size fixed for the cosine-bell example. A right-angled triangular grid with a resolution of $N = 256$ is employed to

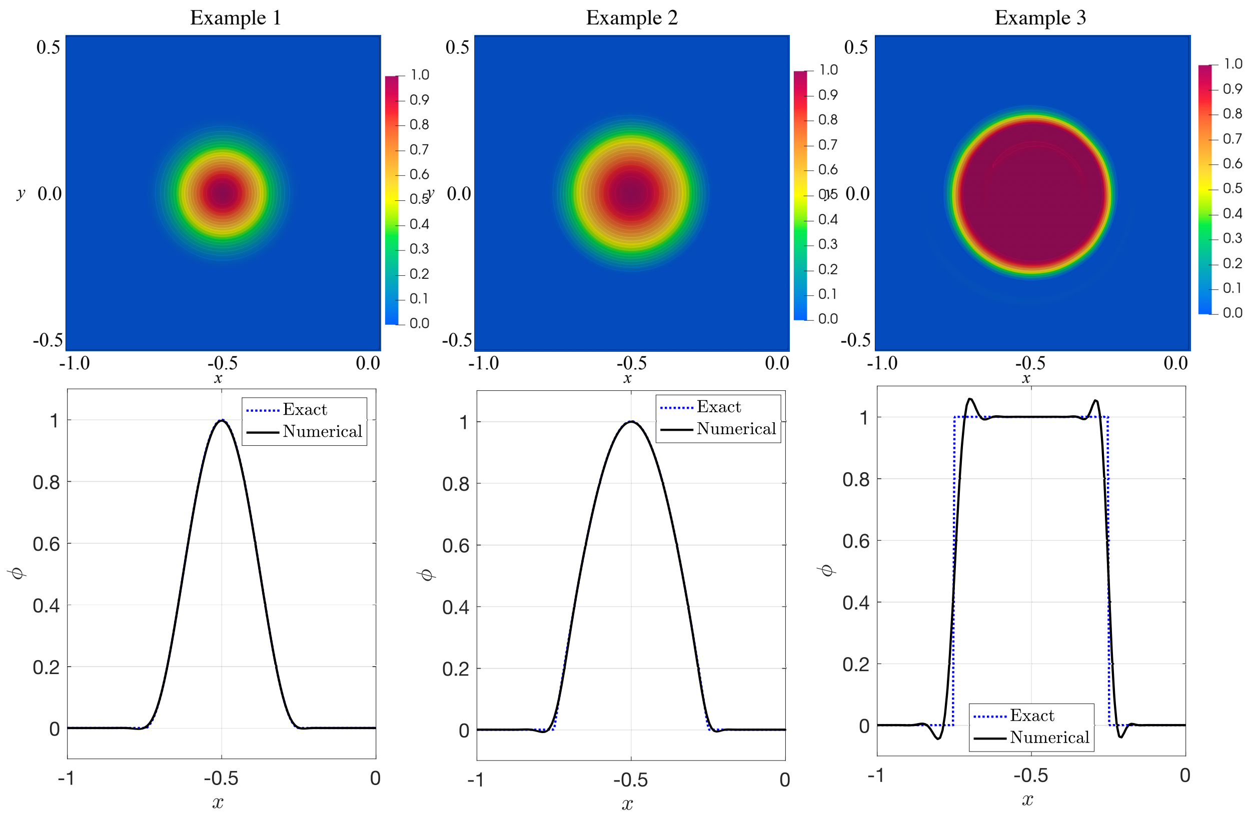


Figure 6: Numerical solution for the 2D solid-body rotation example at $t = 1$ using the three different initial condition and the right-angled triangular grid of $N = 256$. The one-dimensional results are extracted from the line $y = 0$.

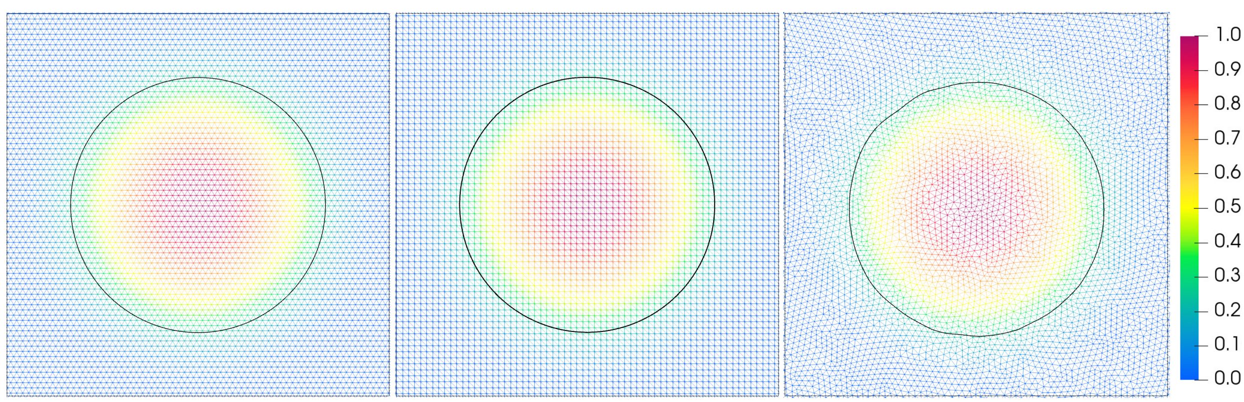

Figure 7: Numerical solution at $t = 1$ of Example 1 using different types of grid ($N = 256$).

minimize spatial errors. Figure 9 presents the errors in both norms for the explicit ($\theta = 0$), implicit ($\theta = 1$), and Crank-Nicolson (C-N) scheme ($\theta = 1/2$). Notably, the C-N scheme achieves spatial accuracy more quickly than the explicit and implicit schemes.

Figure 9 also shows the slope of the regression line for the initial norm errors, confirming that the C-N scheme is second-order accurate, while the explicit and implicit schemes are only first-order accurate in time, as expected. Although the results are not presented here, comparable outcomes

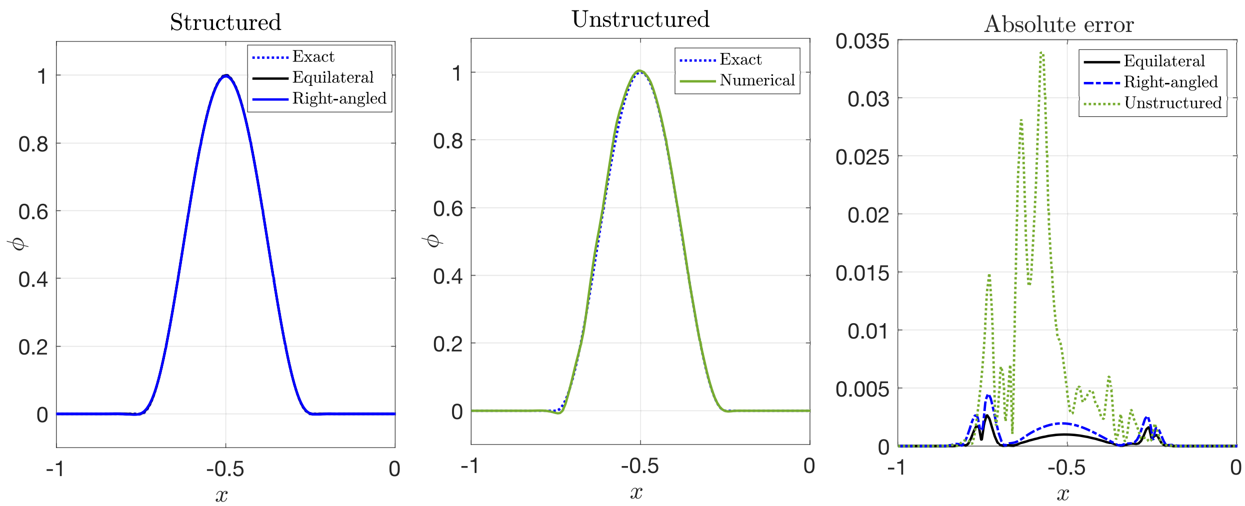


Figure 8: Numerical solution and absolute errors at $t = 1$ and $y = 0$ of Example 1 using different types of grid ($N = 256$).

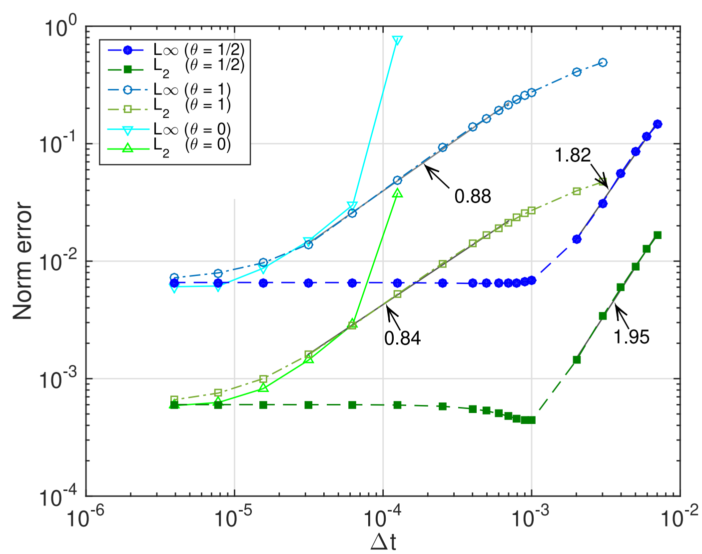


Figure 9: Convergence analysis for the 2D solid-body rotation example at $t = 1$ using different temporal schemes.

are observed using a high-resolution equilateral triangular grid or an unstructured mesh. However, changes in the regularity of the initial condition have a significant effect on the spatial error, which dominates the overall error (combining space and time) in the simulation.

Spatial accuracy is evaluated by varying the grid size while keeping the time step constant. The C-N scheme with a time step of $\Delta t = 10^{-5}$ was selected to ensure that the dominant source of error is spatial. Table 2 compare the norm errors and numerical order of accuracy at $t = 1$ for equilateral and right-angled triangular grids. The convergence analysis shows that the proposed method approaches second-order accuracy with the cosine-bell initial condition. However, as the initial condition becomes less regular, a reduction in accuracy is observed. For instance, a first-order method is obtained using the second example and a zero-order approach for the discontinuous function. This behavior is consistent across the two types of structured grids.

Table 2: Space convergence analysis using structured grids with different initial conditions.

| | Equilateral triangular grid | | | | Right-angled triangular grid | | | |
|---|---|---|---|---|---|---|---|---|
| N | $L_\infty$-norm | Order | $L_2$-norm | Order | $L_\infty$-norm | Order | $L_2$-norm | Order |
| **Example 1** | | | | | | | | |
| 32 | 2.41e-01 | — | 2.23e-02 | — | 3.73e-01 | — | 3.24e-02 | — |
| 64 | 5.18e-02 | 2.22 | 5.76e-03 | 1.95 | 9.37e-02 | 1.99 | 9.21e-03 | 1.81 |
| 128 | 1.31e-02 | 1.98 | 1.46e-03 | 1.98 | 1.83e-02 | 2.36 | 2.25e-03 | 2.03 |
| 256 | 4.81e-03 | 1.45 | 3.94e-04 | 1.89 | 6.51e-03 | 1.49 | 5.89e-04 | 1.93 |
| **Example 2** | | | | | | | | |
| 32 | 1.67e-01 | — | 2.18e-02 | — | 2.10e-01 | — | 3.07e-02 | — |
| 64 | 9.17e-02 | 0.86 | 8.98e-03 | 1.28 | 1.08e-01 | 0.96 | 1.19e-02 | 1.37 |
| 128 | 5.24e-02 | 0.81 | 4.03e-03 | 1.16 | 6.17e-02 | 0.81 | 5.22e-03 | 1.19 |
| 256 | 3.05e-02 | 0.78 | 1.89e-03 | 1.09 | 3.64e-02 | 0.76 | 2.43e-03 | 1.10 |
| **Example 3** | | | | | | | | |
| 32 | 5.96e-01 | — | 8.26e-02 | — | 5.96e-01 | — | 8.89e-02 | — |
| 64 | 5.69e-01 | 0.07 | 6.39e-02 | 0.37 | 5.80e-01 | 0.04 | 6.89e-02 | 0.37 |
| 128 | 5.84e-01 | 0.00 | 4.95e-02 | 0.37 | 5.95e-01 | 0.00 | 5.37e-02 | 0.36 |
| 256 | 5.90e-01 | 0.01 | 3.86e-02 | 0.36 | 5.90e-01 | 0.01 | 4.20e-02 | 0.35 |

In contrast, for the unstructured triangular grid, calculating the order of accuracy becomes more challenging, as the errors depend on both the size and configuration of the mesh, see Fig. 10. Table 3 presents the results at $t = 1$ for unstructured triangular grids of different resolutions. The errors show that the proposed method's error decreases as a finer mesh is used; however, this reduction is less consistent compared to structured grids, as expected. Nevertheless, the same behavior of accuracy loss is observed as the initial condition becomes less regular.

Table 3: Errors using an unstructured triangular grid with different initial conditions.

| | **Example 1** | | **Example 2** | | **Example 3** | |
|---|---|---|---|---|---|---|
| $\Delta x$ | $L_\infty$-norm | $L_2$-norm | $L_\infty$-norm | $L_2$-norm | $L_\infty$-norm | $L_2$-norm |
| 0.0625 | 7.66e-01 | 8.01e-02 | 3.16e-01 | 4.04e-02 | 8.07e-01 | 9.29e-02 |
| 0.03125 | 1.56e-01 | 1.57e-02 | 2.63e-01 | 2.48e-02 | 8.78e-01 | 8.12e-02 |
| 0.015625 | 6.43e-02 | 5.70e-03 | 9.98e-02 | 9.31e-03 | 7.93e-01 | 5.79e-02 |

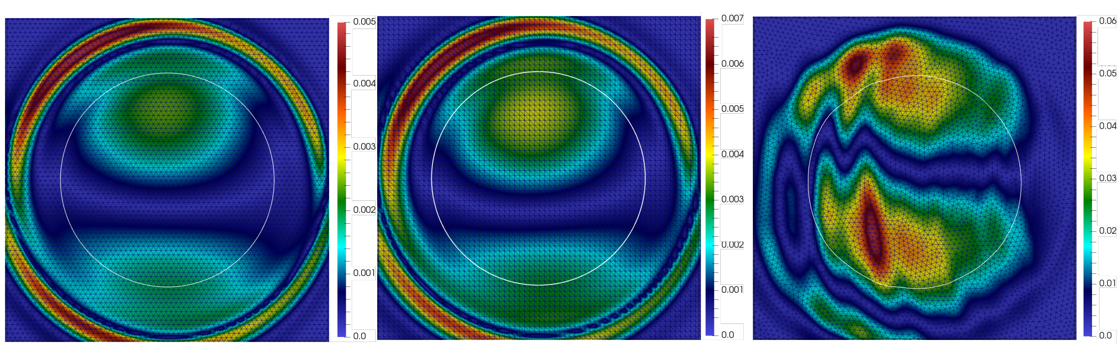


Figure 10: Absolute errors at $t = 1$ using the cosine-bell initial condition and different types of grid with resolution $N = 256$.

### 5.5 Effect of the flux-limiter technique

As shown in Fig. 6, the numerical results with the second-order upwind scheme show small oscillations around the sharp gradient regions for the non-derivable and discontinuous case. In order to eliminate or reduce these errors, we apply the upwind method together with the flux-limiter technique, as described in Section 3.3. Figure 11 shows the numerical solution using this technique at $t = 1$ and the right-angled triangular grid of resolution $N = 256$. As expected, the method with flux-limiter technique gives accurate results and significantly reduces the undesirable oscillations for all cases, showing the advantage of its application.

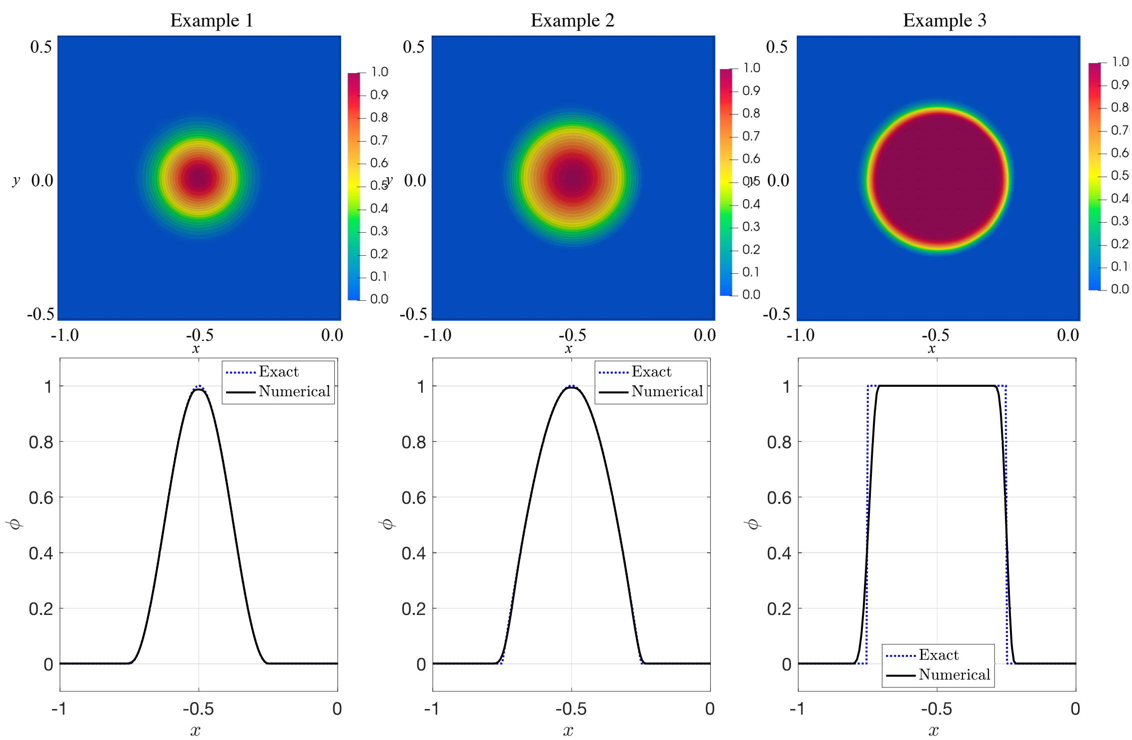


Figure 11: Numerical solution using the flux-limiter technique at $t = 1$. We apply it to the three different initial conditions with the right-angled triangular grid of resolution $N = 256$. The one-dimensional results are extracted from the line $y = 0$.

Conversely, a comparison between Fig. 6 and Fig. 11 reveals a reduction in the maximum values for both Example 1 and Example 2. This reduction is expected, as the use of a flux limiter can effectively dampen sharp gradients, potentially lowering the scheme's accuracy to first-order in regions with high variation. While this behavior helps to mitigate oscillations around discontinuities, it may also slightly smooth out peak values in otherwise stable regions. However, this behavior does not significantly impact the overall order of accuracy, as presented in Table 4. Note that this technique preserves the original order of accuracy of the three examples, as expected.

Figure 12 shows a comparison about the norm errors using the upwind scheme with and without the flux-limiter technique for Example 1. Note that the flux limiter slightly reduces the $L_2$-norm errors compared to the original upwind solution. The maximum error using the flux limiter is larger than the solution without it; however, both remain within the same order of magnitude (share the same slope).

Table 4: Space convergence analysis using structured grids with different initial conditions and the flux-limiter technique.

| | Equilateral triangular grid | | | | Right-angled triangular grid | | | |
|---|---|---|---|---|---|---|---|---|
| N | $L_\infty$-norm | Order | $L_2$-norm | Order | $L_\infty$-norm | Order | $L_2$-norm | Order |
| **Example 1** | | | | | | | | |
| 32 | 3.14e-01 | — | 2.28e-02 | — | 4.67e-01 | — | 3.52e-03 | — |
| 64 | 8.66e-02 | 1.86 | 4.85e-03 | 2.23 | 1.45e-01 | 1.69 | 8.24e-03 | 2.09 |
| 128 | 2.56e-02 | 1.76 | 1.22e-03 | 1.99 | 4.05e-02 | 1.84 | 1.84e-03 | 2.16 |
| 256 | 7.62e-03 | 1.75 | 3.50e-04 | 1.80 | 1.21e-02 | 1.74 | 4.95e-04 | 1.89 |
| **Example 2** | | | | | | | | |
| 32 | 1.52e-01 | — | 2.02e-02 | — | 2.79e-01 | — | 3.10e-02 | — |
| 64 | 7.59e-02 | 1.00 | 7.58e-03 | 1.41 | 8.48e-02 | 1.72 | 9.90e-03 | 1.65 |
| 128 | 4.72e-02 | 0.69 | 3.24e-03 | 1.23 | 5.48e-02 | 0.63 | 4.24e-03 | 1.22 |
| 256 | 2.93e-02 | 0.69 | 1.47e-03 | 1.14 | 3.34e-02 | 0.71 | 1.92e-03 | 1.14 |
| **Example 3** | | | | | | | | |
| 32 | 5.89e-01 | — | 8.11e-02 | — | 5.80e-01 | — | 8.81e-02 | — |
| 64 | 5.52e-01 | 0.09 | 6.19e-02 | 0.39 | 5.78e-01 | 0.00 | 6.70e-02 | 0.39 |
| 128 | 5.63e-01 | 0.00 | 4.73e-02 | 0.39 | 5.61e-01 | 0.04 | 5.16e-02 | 0.38 |
| 256 | 5.49e-01 | 0.04 | 3.63e-02 | 0.38 | 5.49e-01 | 0.03 | 3.99e-02 | 0.37 |

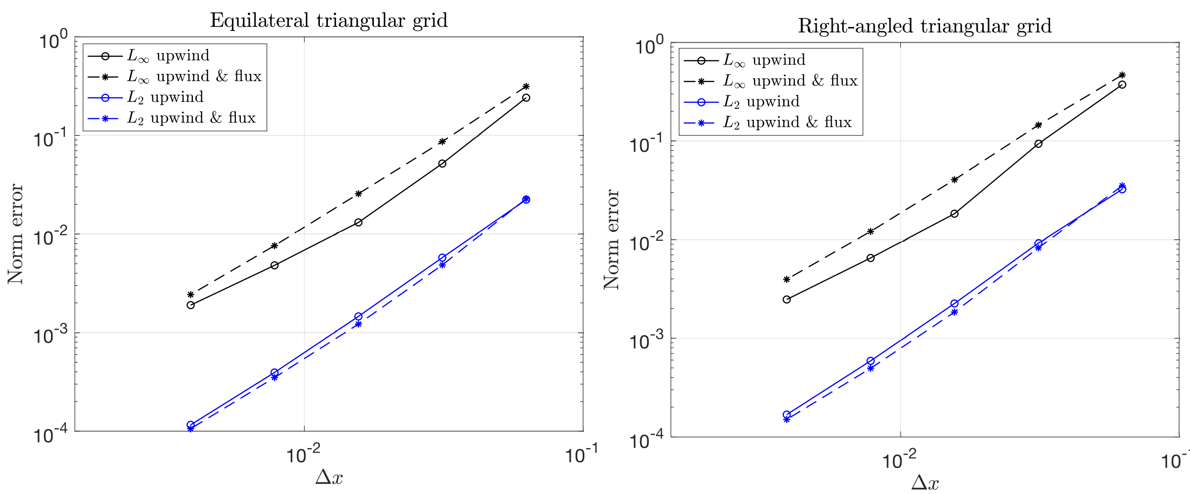


Figure 12: Convergence analysis for Example 1 at $t = 1$ using different structured grid resolutions.

# 6 Conclusions

In this paper we have presented a second-order discretization for the conservative transport equation based on an unstructured finite-volume method. The results of the discretization are supported by numerical tests, which verify the second-order accuracy in time and in space. However, there is an important influence of the unstructured grid in the precision of the method. As expected, the proposed method performs well for smooth initial functions. Conversely, initial functions with discontinuities or sharp gradient regions, as the Heaviside function, still perform well by only applying a flux-limiter technique. Future work involves the implementation of these techniques to complex interface problems. We will also develop a code to obtain three-dimensional simulations on irregular domains using the proposed finite-volume formulation.

## 7 Acknowledgments

This work was partially supported by the Secretaría de Ciencia, Humanidades, Tecnología e Innovación (SECIHTI) under the program *Investigadores e Investigadoras por México*, and SECIHTI México under Ciencia de Frontera Project Number: CF-2023-I-2639. We also acknowledge to the supercomputer facilities provided by CIMAT, specifically Cluster Merida TOLOK, for their invaluable support in conducting our research.

## 8 Declaration of interests

The authors declare that they have no known competing financial interests or personal relationships that could have appeared to influence the work reported in this paper.

## 9 Declaration of the use of generative artificial intelligence

During the preparation of this work, the authors used ChatGPT to check the grammar of a few paragraphs. After using this tool, the authors reviewed and edited these paragraphs as needed and took full responsibility for the final publication.

## 10 Graphical Abstract

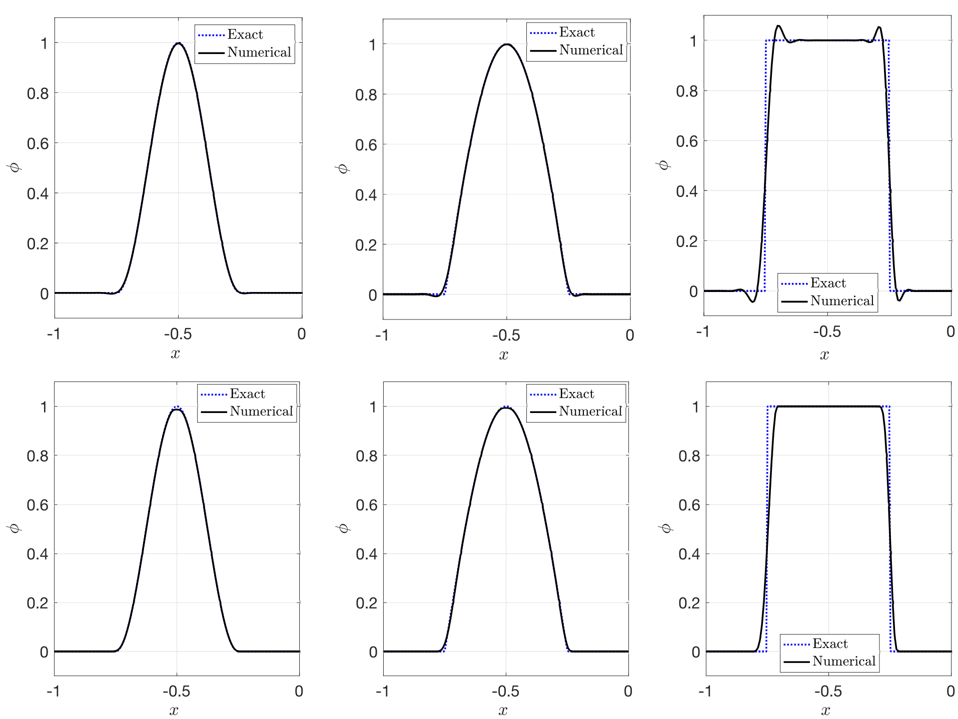


Figure 13: The one-dimensional results are extracted along the line $y = 0$ for both upwind schemes: with the flux limiter technique (first horizontal line) and without it (second horizontal line).

# References


[1] LeVeque RJ. High-resolution conservative algorithms for advection in incompressible flow. SIAM Journal Numerical Analysis, 1996; 33(2):627-65.

[2] Osher S, Fedkiw RP. Level set method: an overview and some recent results. J. Comput. Phys. 2001; 169:463-502.

[3] Sethian JA, Smereka P. Level set methods for fluids interfaces. Annu. Rev. Fluid Mech. 2003; 35:341-372.

[4] Uh Zapata, M., Itzá Balam, R. A conservative level-set/finite-volume method on unstructured grids based on a central interpolation scheme. J. Comput. Phys., 444, 110576, 2021.

[5] Uh Zapata, M., Itzá Balam, R. A 3D Two-Phase Conservative Level-Set Method Using an Unstructured Finite-Volume Formulation. In Mathematical and Computational Models of Flows and Waves in Geophysics (pp. 67-101). Springer International Publishing, 2022.

[6] Kees CE, Akkerman I, Farthing MW, Bazilevs Y. A conservative level set method suitable for variable-order approximations and unstructured meshes. J. Comput. Phys., 2011; 230:4536-4558.

[7] Ito K, Kunugi T, Ohshima H, Kawamura T. (2013). A volume-conservative PLIC algorithm on three-dimensional fully unstructured meshes. Computers & Fluids, 2013; 88, 250-261.

[8] Balcázar N, Jofre L, Lehmkuhl O, Castro J, Rigola J. A finite-volume/level-set method for simulating two-phase flows on unstructured grids. International journal of multiphase flow, 2014; 64:55-72.

[9] Xie B, Peng J, Feng X. An unstructured-grid numerical model for interfacial multiphase fluids based on multi-moment finite volume formulation and THINC method. International Journal of Multiphase Flow, 2017; 89:375-398.

[10] Li LX, Liao HS, Qi LJ. An improved r-factor algorithm for TVD schemes. International Journal of Heat and Mass Transfer, 2008; 51(3-4):610-617.

[11] Lien FS. A pressure-based unstructured grid method for all-speed flows, Int. J. Numer. Meth. Fluids 2000; 33:355-374.

[12] Vidović D, Segal A, Wesseling P. A superlinearly convergent Mach-uniform finite volume method for the Euler equations on staggered unstructured grids. Journal of Computational Physics 2006; 217(2):277-294.

[13] Eymard R, Gallouet T, Herbin R. Finite Volume Methods, Handbook of numerical analysis, Vol. VII, Handb. Numer. Anal.,VII, North-Holland, Amsterdan 2000.